Article

Manipulation of Mg2+- Ca2+ switch on the development of bone mimetic hydroxyapatite

Nancy C. Andrés, Noelia L. D'Elía, Juan M. Ruso, Adrián Esteban Campelo, Virginia L. Massheimer, and Paula V. Messina

ACS Appl. Mater. Interfaces, **Just Accepted Manuscript** • Publication Date (Web): 20 Apr 2017

Manipulation of Mg^{2+}- Ca^{2+} switch on the development of bone mimetic hydroxyapatite

*Nancy C. Andrés [a§], Noelia L. D´Elía [a§], Juan M. Ruso [b], Adrián E. Campelo[c], Virginia L. Massheimer[c], Paula V. Messina [a]**

(a) INQUISUR – CONICET, Department of Chemistry, Universidad Nacional del Sur, B8000CPB, Bahía Blanca, Argentina. (b) Soft Matter and Molecular Biophysics Group, Department of Applied Physics, University of Santiago de Compostela, Santiago de Compostela, 15782, Spain. (c) INBIOSUR - CONICET, DBByF, Universidad Nacional del Sur, B8000ICN, Bahía Blanca, Argentina

* Author to whom correspondence should be addressed. Tel: +54 291 4595159. Fax: +54 291 4595160. Electronic mail: pmessina@uns.edu.ar.

§ These authors contributed equally to this work, and should be considered as co-first authors.

Keywords: Magnesium substitution; hydroxyapatite; calcified tissues; cell proliferation

Abstract. Ionic substitution can affect essential physicochemical properties leading to a specific biological behavior upon implantation. Therefore it has been proposed as a tool to increase the biological efficiency of calcium phosphate based materials. In the following study we have evaluated the contribution of an important cation in nature, Mg^{2+}, into the structure of previously studied biocompatible and biodegradable hydroxyapatite (HA) nano-rods and its subsequent effect on its chemical, morphology and bone mimetic articulation. Mg^{2+}-substituted HA samples were synthesized by an aqueous wet-chemical precipitation method followed by an hydrothermal treatment involving a Mg^{2+} precursor that partially replace Ca^{2+} ions into HA crystal lattice; Mg^{2+} concentrations were modulated to obtain a nominal composition similar to that exists in calcified tissues. Hydrothermally-synthesized Mg^{2+}-substituted HA nanoparticles were characterized by X-ray powder diffraction, FT-NIR and EDX spectroscopies, field emission scanning and high resolution transmission electron microscopies (FE-SEM, H-TEM). Molecular modeling combining *Ab Initio* methods and power diffraction data were also performed. Results showed that Mg^{2+}-substitution promoted the formation of calcium deficient HA (cdHA) where Mg^{2+} replacement is energetically favored at Ca(1) position in a limited and specific amount directing the additional Mg^{2+} toward the surface of the crystal. The control of Mg^{2+} incorporation into HA nano-rods gave rise to a tailored crystallinity degree, cell parameters, morphology, surface hydration, solubility and degradation properties in a dose-replacement dependent manner. The obtained materials show qualities that conjugated together to drive an optimal *in vitro* cellular viability, spreading and proliferation confirming their biocompatibility. In addition, an improved adhesion of osteoblast was evidenced after Mg^{2+}- Ca^{2+} substitution.

1. Introduction

Notwithstanding the steady advances in material science field, the creation of calcium phosphate (CaP) ceramics analogous to the mineral matrix of calcified tissue remains one of the most ambitious goals of implants research, mainly due to the difficulty of simultaneously mimic the morphology and microstructure thereof.[1] In accordance to the biomimetic principle, an implant should seem as closely as possible the host tissue to be replaced. Thus, the optimal CaP biomaterial applied for hard tissue repair should consist of nanometric, hierarchically structured and poorly crystallized hydroxyapatite (HA) distinguished by a non-stoichiometric composition.[2] In previous works [3-4] we successfully fabricated biocompatible HA nano-rods possessing a precise chemical composition, controlled crystalline dimensions, an accurate hydrophilic surface and an optimal degradation rate under cell-mediated acidic conditions; features that allow a normal growth and differentiation of bone cells *in vitro*. Furthermore the evaluation of the interaction between HA nano-rods with hydrolyzed collagen peptide units was done. In the course of the study, HA nano-crystals affected the hydrodynamic environment of the protein network producing hybrid scaffolds with improved mechanical and thermal stability properties. [5-6] The assimilation of HA nanoparticles, also stimulate an improved mineralization of the scaffold [6] and an accelerated platelet-poor plasma burst coagulation in a dose-dependent manner.[7]

In the present work a further step was taken towards the construction of synthetic materials that resemble calcified tissues, and for this reason the ionic substitution present in the biogenic apatite was introduced.[8] In particular, it was explored the magnesium ion (Mg^{2+}) substitution because it is quantitatively one of the most significant bivalent ions present in biological apatite.[9] The Mg^{2+} content in enamel, bone and dentin are about 0.44, 0.72, 1.23

wt % respectively; [9-10] its depletion in calcified tissues harmfully affects all stages of skeletal metabolism, producing the disruption of bone augmentation, a decrease of osteoblast activity, osteopenia and bone fragility.[11-12] This article is focused on Mg^{2+} - Ca^{2+} switch in HA nanoparticles prepared at room temperature (RT) and its effect on the microstructural and morphological features to attain bone repair. In the first part of the work, the main characteristics of Mg^{2+}- HA nanoparticles are correlated with the modifications induced by ionic substitution. Experimental and theoretical approaches are brought together to examine the effects of Mg^{2+} substitution on the apatite organization, its average particle size, morphology, crystallinity degree and unit cell parameters. Furthermore, it is recognized that the substitution of Ca^{2+} positions by Mg^{2+} in the surface of the crystal induces a chaotic state where ions are constantly swapped from the outer hydrated layer and expands the number of molecular layers of coordinated water; [13-14] all these events affect the material resorption abilities as well as its protein adsorption capacity and future cells adhesion. Thus, our study follows with the analysis of Mg^{2+} substitution effect on the material hydrophilicity and degradation properties under osseous resorption conditions correlating the ion release with its biocompatibility in the presence of osteoblasts and endothelial cells.

The results obtained from this work would contribute to a better understanding of the ionic substitution effect on the properties of precipitated phases and, consequently, to the design of raw materials for tissue engineered implants displaying enhanced bioactivity and specific ionic delivery abilities to treat bone diseases.

2. Experimental

2.1 Reagents

Hexadecyl-trimethyl ammonium bromide (CTAB, 99 % Sigma-Aldrich), poly (propylene glycol) (PPG, MW = 425 g mol^{-1}, δ = 1.004 g cm^{-3} at 25ºC, Sigma-Aldrich), sodium phosphate (Na_3PO_4, 96 % Sigma-Aldrich), calcium chloride ($CaCl_2$, 99 % Sigma-Aldrich), magnesium chloride hexahydrate ($MgCl_2 \bullet 6H_2O$, 99 % Sigma-Aldrich); sodium nitrite ($NaNO_2$, 97% Sigma-Aldrich), acetic acid ($C_2H_4O_2$, 99 % Sigma-Aldrich), sodium acetate tri-hydrate ($C_2H_3NaO_2 \bullet 3H_2O$, 99 % Sigma-Aldrich), phosphate buffer saline (PBS tablets, Sigma-Aldrich), lysozyme from chicken egg (LSZ for molecular biology, Sigma-Aldrich) and sodium azide (NaN_3, 99.5 %, Sigma-Aldrich) were used without further purification. For biocompatibility assays, Dulbecco's Modified Eagle's Medium (DMEM, Sigma-Aldrich); Alpha-Minimum Essential Medium (α-MEM, Sigma-Aldrich); fetal calf serum (FCS, Sigma-Aldrich); penicillin (PE, BioReagent, Sigma-Aldrich); amphotericin-B solution (AMP-B, 250 μg cm^{-3} in deionized water, sterile-filtered, BioReagent, Sigma-Aldrich); L-glutamine (L-GLU, 200 mM, solution, sterile-filtered, BioXtra, Sigma-Aldrich); ethylenedinitrilotetraacetic acid (EDTA, Sigma-Aldrich); collagenase from *Clostridium histolyticum* for general use (COLL, Type I, 0.25-1.0 FALGPA units mg^{-1} solid, ≥125 CDU mg^{-1} solid, Sigma-Aldrich); albumin (Sigma-Aldrich); streptomycin sulfate salt (STREP, BioReagent, Sigma-Aldrich); ascorbic acid (AA, Sigma-Aldrich); β-glycerophosphate disodium salt hydrate (β-GLY, BioUltra, Sigma-Aldrich); Triton X-100 (TX-100, Sigma-Aldrich); crystal violet powder (CV, Sigma-Aldrich); 4′,6-Diamidine-2′-phenylindole dihydrochloride (DAPI, Sigma-Aldrich); dimethyl sulfoxide (DMSO, δ = 1,1 g cm^{-3} at 25°C, 99 % Sigma-Aldrich); absolute ethanol (EtOH, δ = 0,78 g cm^{-3} at 25°C, 99 %, Sigma-Aldrich); paraformaldehyde (PFA, monomer, Sigma-Aldrich) and sodium

bicarbonate ($NaHCO_3$, 99.5 %, Sigma-Aldrich) were used. For solutions preparation, only sterile Milli-Q® water was used. For all tests passage two (P2) cells were used.

2.2 Mg^{2+}- HA nanoparticles preparation

The rule of synthesizing bivalent Mg^{2+} cation substituted HA employing a wet-chemical precipitation method is stated by the following equation:

$$(10\text{-}x)\ Ca^{2+} + x\ Mg^{2+} + 6\ PO_4^{3-} + 2OH^- \rightarrow Ca_{(10-x)}Mg_x(PO_4)_6(OH)_2 \qquad (0 \leq x \leq 10)$$

Four materials (denoted as MgI-HA, MgII-HA, MgIII-HA and MgIV-HA) were prepared using a modification of a previously described methodology: [3] 350 mL of a 3.14 mM CTAB aqueous solution was placed in contact with 20 mL of PPG and stirred at 500 rpm during 10 min. Then, 200 mL of 2 M $NaNO_2$ solution, 208.9 mg calcium chloride and 11.9 mg (MgI-HA), 20.2 mg (MgII-HA), 40.3 mg (MgIII-HA), 201.6 mg (MgIV-HA) of magnesium chloride hydrate were integrated in sequence. Finally, 200 mL of 0.14 M Na_3PO_4 aqueous solution was added drop by drop at RT to the previous mixture with continuous magnetic stirring at 500 rpm. Once all reactants were assimilated, the suspension was magnetically stirred for 1h. The gels obtained were left for 24 h in an autoclave at 100ºC. To finish, the powders were filtered and washed with Milli-Q® water to avoid contamination; surfactant was completely eliminated by calcination at 400°C during 3 h under air flux.

2.3 Structural characterization

2.3.1 Field emission scanning electron microscopy (FE-SEM). The surface characterization was performed using a FE-SEM ZEISS ULTRA PLUS coupled to an X-ray energy-

dispersive (EDX) spectrophotometer. Images were acquired with a secondary electron detector (In lens) operated at an accelerating voltage (EHT) of 3.00 kV and at a working distance (WD) resolution of 2.1 nm. Local compensation of charge was achieved by injecting nitrogen gas.

2.3.2 Transmission electron microscopy (TEM). TEM was achieved using a Philips CM-12 microscope coupled to a digital camera MEGA VIEW-II DOCU operating at a voltage of 120 kV and displaying a maximum magnification of 730000×. High resolution (H-TEM) microphotographs were acquired using a Libra 200 FE OMEGA microscope working at 200 kV of operating voltage that corresponds to a maximum magnification of 1000000×. Powdered samples were situated on cooper and carbon supports of 2000 mesh as required and observations were made in a bright field.

2.3.3 X-ray powder diffraction (XRD). XRD data were acquired with a Philips PW 1710 diffractometer associated to a Cu K_α radiation source (λ = 1.5418 nm) and a graphite monochromator operated at 45 kV; 30 mA and 25ºC. The average crystalline size (δ_{hkl}) was calculated based on the Scherrer formula by the following equation: [15]

$$\delta_{hkl} = \frac{0.9\,\lambda}{\cos\theta\sqrt{\left(\omega^2 - \omega_0^2\right)}} \qquad (1)$$

where λ is the wavelength (Cu K_α), θ is the diffraction angle, ω is the experimental full-width at the half maximum (FWHM) obtained for each sample and ω_0 is the standard FWHM value. To calculate the average crystal size along to the crystallographic axis *c* and *a*, respectively, the FWHM at 2θ = 25.8° and 33.1° corresponding to (002) and (300) Miller plane family of HA (JCPDS file #09-0432) were chosen.[15] The fraction of crystalline phase (X_c) was also calculated: [16]

$$X_c = 1 - \frac{v_{112/300}}{I_{300}} \quad (2)$$

where I_{300} is the intensity of (300) diffraction peak and $\upsilon_{112/300}$ is the intensity of the hollow between (112) and (300) diffraction peaks of HA. Verification was done with the relation:[17]

$$B_{002}\sqrt[3]{X_c} = K \quad (3)$$

where K is a constant found equal to 0.24 for a very large number of different HA powders,[10] and B_{002} is the FWHM (in degrees) of the (002) reflection. The estimated uncertainties are about 20 %. Of the two known allotropic forms of HA (monoclinic, space group $P2_1/b$, and hexagonal, space group $P6_3/m$), only the hexagonal phase is of practical importance because the monoclinic form is destabilized by the presence of even small amounts of foreign ions.[2] Considering that it has been confirmed the existence of ionic substitution in the biogenic HA, [2] it was expected that hydroxyapatite crystals correspond to the hexagonal crystal family ($a = b \neq c$; $\alpha = \beta = 90^o$; $\gamma = 120°$). The lattice geometry parameters (*a, c)* and the volume of the direct unit cell *(V),* were computed on basis of the following equation[18] by Rietveld refinement using the Rietica v4.2 software package: [19]

$$\frac{1}{(d_{hkl})^2} = \left[{}^4/_3\right]\left[(h^2 + hk + k^2)/a^2\right] + \left[l^2/c^2\right] \quad (3)$$

$$V = \left[{}^{\sqrt{3}}/_2\right]\left[a^2 c\right] \quad (4)$$

where, d_{hkl} is the interplanar spacing computed by the Bragg equation ($\lambda = 2d_{hkl}\ sen\ \theta$) and (*hkl*) are the Miller index of the symmetric reflections used in the calculus.[18] Molecular modelling were performed by a combined *Ab Initio* method and powder diffraction data [20] using the Endeavour software package (demo version).

3.3.4 Near infrared spectroscopy (FTIR – NIR). A Nicolet iS50 FTIR - NIR spectrophotometer (Thermo Scientific, Waltham, MA, USA) together with a diffuse

reflectance accessory (DRA, also called an integrating sphere), operating in the reflectance mode (λ = 1000 – 2500 nm), at air atmosphere and at RT were used to quantify the reflectance of the powders. For measurements, the samples were maintained inside flat bottom glass vials to form pellets of 10 mm diameter and 5 mm thick and a Gold NIR Diffuse Reflection Standard (99.9 % reflective) was used as a reference to calibrate the baseline.

2.4 In vitro hydrolytic and enzymatic degradation

Each sample was weighted (W_0), 200 mg, and deposited in crystal vessels having 50 mL of PBS (pH = 7.4, containing 0.05 % w/w of NaN_3). Following, they were incubated at 37 ± 0.1 °C throughout 12 days; PBS was refreshed every 3 days. At each time point, samples were collected in triplicate, cleaned carefully with Milli-Q® water, blotted with filter paper, and oven-dried until constant weight (W_t). Taking into consideration that during the bone remodeling period, the vicinity of the ruffled border of osteoclasts have a pH about 4.0 to 5.0, [21] the *in vitro* degradation under acidic conditions was assessed by soaking scaffolds in an acetic acid/sodium acetate buffer solution (AcOH buffer, pH = 4.24) following the method of Matsumoto *et al*. [22] Enzymatic degradation was carried out likewise to the hydrolytic procedure after incorporation of lysozyme (LSZ) into PBS to form an enzymatic degradation environment (13 mg dm^{-3}). This concentration was chosen reassembling to the normal LSZ concentrations in plasma.[23] The degradability of Mg^{2+}- HA samples was computed from the rate of weight loss (*% W_L*) following the Tampieri *et al.*[24] methodology:

$$\% W_L = \frac{(W_0 - W_t)}{W_0} \times 100 \quad (6)$$

Supernatant Ca^{2+} concentrations were determined by inductively coupled plasma-atomic emission spectrometry (ICP-AES) using the method 6010C (EPA, 2007). The solubility product (K_{sp}) at 37°C and pH = 7.4 was calculated from the obtained data after 10 days of treatment, since 5 days seems to be adequate to reach a relatively stable and horizontal slope in the dissolution curve, [25] **figure S1** of supporting information (SI).

2.5 Biocompatibility assays

2.5.1 Mg^{2+}- HA nanoparticles dispersions. Prior to use, Mg^{2+}- HA powders were sterilized in an autoclave at 121°C during 20 min. Then a sterile material dispersion in culture media (4.0 mg cm^{-3}) was prepared by placing the components on a rotating mixer for 15 min. The properly amount of culture media material dispersion was used to have a final cytocompatible level of Mg^{2+}- HA nanoparticle of 7.14 μg / well. [4]

2.5.2 Rat endothelial cells (rECs) and osteoblasts (rOBs) isolation and culture. Primary cultures of rECs and calvaria rOBs were acquired from aortic rings explants and calvarias respectively isolated from young Wistar rats as previously described. [26, 27, 3] Animals were kept at uniform temperature (22 ± 1°C) and humidity (70 %) conditions, in 12 h dark cycles with free access to tap water and standard diet throughout all the experiment. Animals' care and handling were performed by the animal service of the Department of Biology, Biochemistry and Pharmacy - Universidad Nacional del Sur – Argentina in agreement with the internationally recognized standard Guide for the Care and Use of Laboratory Animals promulgated by the National Research Council. [28] The active procedures used in this work have been approved by the CICUAE (Institutional Committee for the Care and Use of

Experimental Animals, Biology, Department of Biology, Biochemistry and Pharmacy of the Universidad Nacional del Sur – Argentina).

2.5.3 Mitochondrial Metabolic Activity, cells morphology and viability. Mitochondrial metabolic activity, and indirectly the cells viability, [29-30] after 48 h of culture in the presences of Mg^{2+}- HA nanoparticles were evaluated using a MTT assay kit (Sigma-Aldrich), as described by Denizot and Lang.[31] For the experiments, cells ($1x10^4$ cells / well) were seeded onto a 96-well plate, flat bottom, and incubated with 7.14 μg / well of Mg^{2+} - HA nanoparticles for 48 h in 100 μL of DMEM with 2 % (v/v) FCS. Cells cultured in the absence of the material (C) and non-substituted HA were used as controls. After treatment, 10 μL of MTT reagent were added to each sample and the plate was incubated in darkness at 37 ºC under a 5 % CO_2 atmosphere for 4 h. The medium was then removed and 100 μL of DMSO were added to each well. Absorbance was measured at λ = 505 nm in a multiplate reader (Sinergy-HT Biotek) using a λ = 700 nm as blank reference. Results are expressed as optical density percent (O.D. %). Finally, the cells were observed and microscopic photographs were taken in a phase contrast inverted microscope Nikon eclipse TS100 coupled to a Nikon D3200 camera.

To evaluate the cell morphology and adherence in the presence of the Mg^{2+}- HA nanoparticles, the samples were then extended on a microscope slide, air dried, fixed with absolute ethanol and stained with CV. [32] Experiments were performed with two different cell preparations and repeated five times. Cytomorphometric analysis was done using free Image J (National Institutes of Health, Bethesda, MD) software accordingly to the Foldberg *et al.* methodology. [33] For the determination of cellular area and its length, each cell was considered an object equivalent to an ellipse. [33] Then, the aspect ratio of each cell was

estimated by dividing the major axis of the ellipse by the minor. Only cells that were entirely included in the field of vision and exhibited a well-defined cellular and nuclear outlines were selected. The average values of cellular area and diameters of a 20 cells were obtained and recorded.

2.5.4 Immunofluorescence test. rOBs and rECs were cultured during 48h on 96-well optical bottom glass-based plates (Nunc Cat. 164588) in the presence of 7.14 μg / well of Mg^{2+}-HA nanoparticles. Cells were processed as previously described.[34] Non confluent cultures cells were fixed with 3 % (w/v) PFA solution and permeabilized with 0.1 % (w/v) TX-100 for 5 min; blocking was performed with 3 % (w/v) albumin in PBS for 30 min. Nuclei were counterstained with DAPI. Images were acquired using an Olympus BX41 fluorescence microscope with excitation filter set in the ultraviolet (330-385nm). All images, recorded with an Olympus Q Color 3 digital camera, were analyzed using the software Image J (National Institutes of Health, Bethesda, MD). Amount of cells was determined by counting positive nucleus for DAPI stain in a histology field per sample.

2.6 Statistical analysis

All quantitative assessments were taken in triplicate, and results are expressed as mean ± standard deviation (SD). Statistical analysis of data was realized by one factor analysis of variance (ANOVA). Student's *t*-test and probability values below 0.05 ($p < 0.05$) were considered as a significantly difference.

3. Results and discussion

3.1 Mg^{2+}- substituted apatites

3.1.1. Chemical biomimesis. Mg^{2+}- substitution influence on the apatite crystalline microstructure

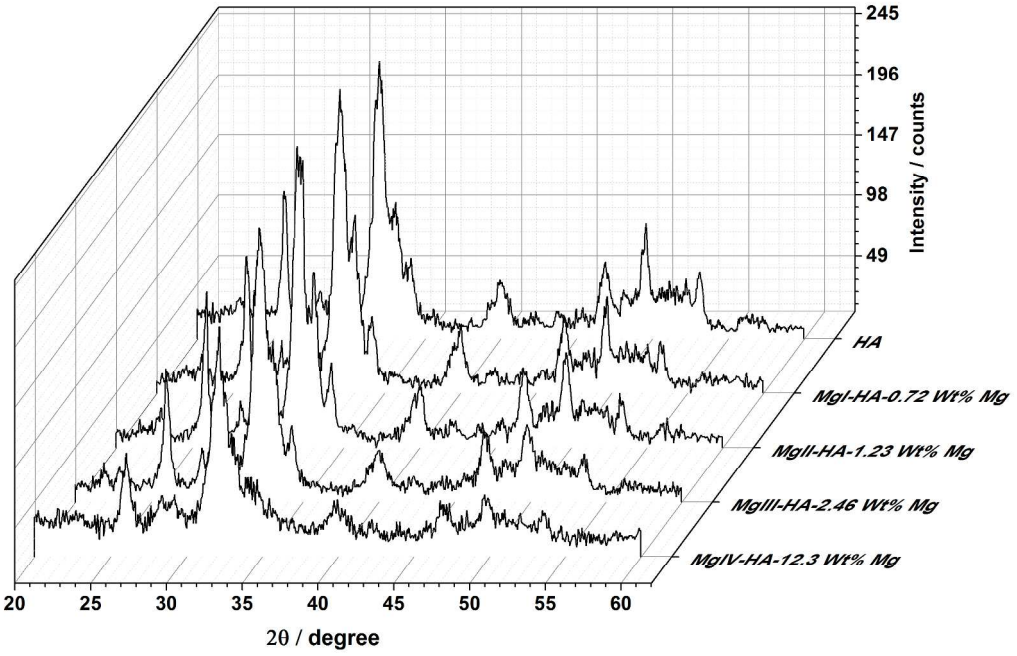

Figure 1. XRD pattern of dried Mg^{2+}-substituted HA

Mg^{2+}- substituted hydroxyapatite powders (Mg^{2+}- HA) of different composition were prepared supposing that Mg^{2+} ions would switch the calcium position in the HA lattice in order to obtain a nominal concentration equivalent to that exists in bone (MgI-HA) and dentin (MgII-HA); materials containing two to ten times the amount of Mg^{2+} in dentin are also formulated (MgIII-HA and MgIV-HA) to evaluate the maximum capacity of Mg^{2+}-substitution into de HA framework. **Table 1** shows the Ca/Mg molar ratio of starting synthesis solutions and the final values of the manufactured materials obtained by EDX microanalysis; please refer to **figures S2-S5** of SI. The Ca/Mg molar ratios in the final apatite products were slightly different than those in the initial synthesis solutions; effective Mg^{2+} incorporation was about 75 ± 5 mol%.

Inset Table 1, here

XRD patterns of as-dried Mg^{2+}- HA powders are compared in **figure 1**; all XRD spectra showed reflections associated with poor crystallized hydroxyapatite, showing a comparable pattern of peaks than calcium deficient hydroxyapatite (cdHA) existing in calcified tissues.[35] No peaks insinuating the presence of additional calcium phosphate polymorphs or Mg^{2+}- crystalline phases were detected, however broad bands typical of amorphous calcium phosphate (ACP) [36] are evident. In good agreement with literature results, [10] the crystallinity degree progressively decreased as the Mg^{2+}- substitution increase; particularly the high Mg-substituted samples show a crystallinity degree comparable to calcified tissue samples, [37] **table 2.** Despite of X-ray diffraction profiles similarity, slight divergences can be observed from the examination of interplanar *d*-spacing and the calculated crystallographic parameters, **figure 2**. These differences undoubtedly derive from Ca^{2+}-Mg^{2+} replacement and clearly influenced the physical properties of the materials. The mean crystallite size (δ_{hkl}) of non-substituted HA sample, computed by equation (1), was about 44 ± 8 nm and 22 ± 4 nm along *c* and *a* axis respectively, while a clear size reduction along *a* axis can be appreciated due to Mg^{2+}- substitution, **table 2**.

Insert table 2, here

The determined cell dimensions along *c* and *a* axis, **figure 2,** and the direct unit cell volume (*V*) associated, **table 2**, confirmed the contraction of lattice parameters along *a* axis that is a result of the smaller ionic radius of Mg^{2+} contrasted with Ca^{2+}. [10, 38] Due to the reduction of the *a* crystallographic dimension, the *c/a* ratio that correspond to the Mg^{2+}- HA samples ($c/a = 0.7319 \pm 1.4 \times 10^{-3}$) is superior to the *c/a* ratio of non-substituted HA sample (*c/a* =

0.7297), but it is statistically comparable to the biogenic apatite value reported for adult bone and dentin, $c/a = 0.7321$ and $c/a = 0.7310$ respectively, [37] **table 2**.

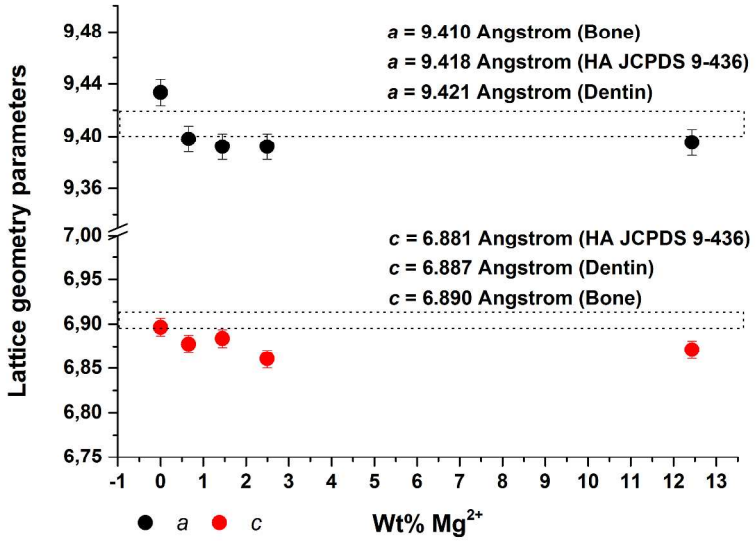

Figure 2. Computed crystallographic parameters as a function of Mg^{2+}- substitution. The black dot lines represent the ranges corresponding to stoichiometric and biogenic HA values.

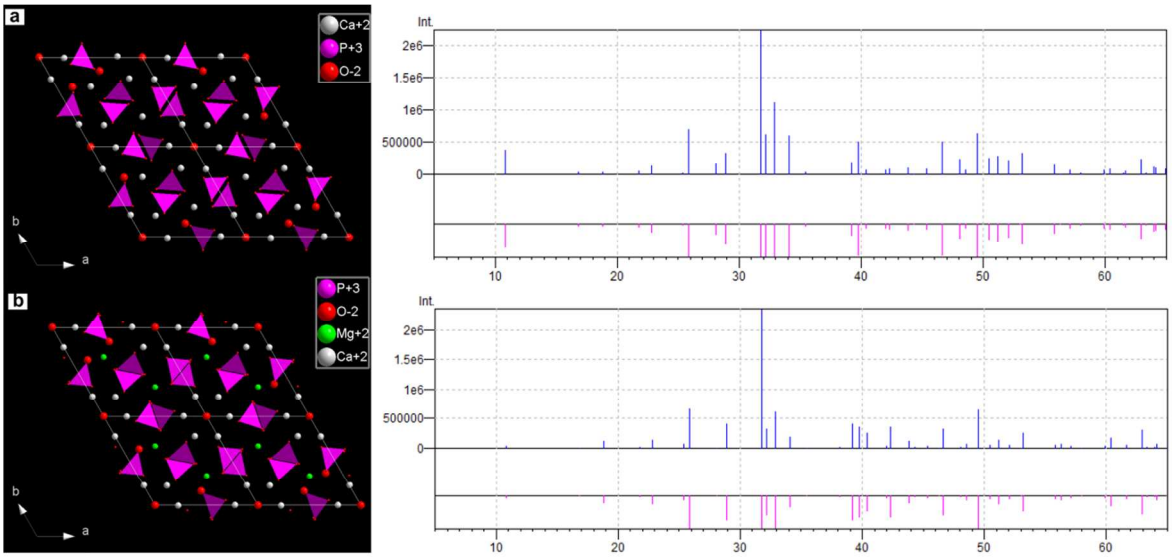

Figure 3: Theoretical model of **(a)** stoichiometric HA (Ca10P6O23) and **(b)** Mg^{2+}- HA (Ca6Mg4P6O23) unit cell and the associated X-ray diffraction pattern.

The rigorous position of the Mg^{2+} ions in HA framework is an unresolved problem. [38] Whether Mg^{2+} ions partially replace their calcium counterparts in apatite lattices or if they are situated on the surfaces of the apatite crystals is a controversial subject.[39]

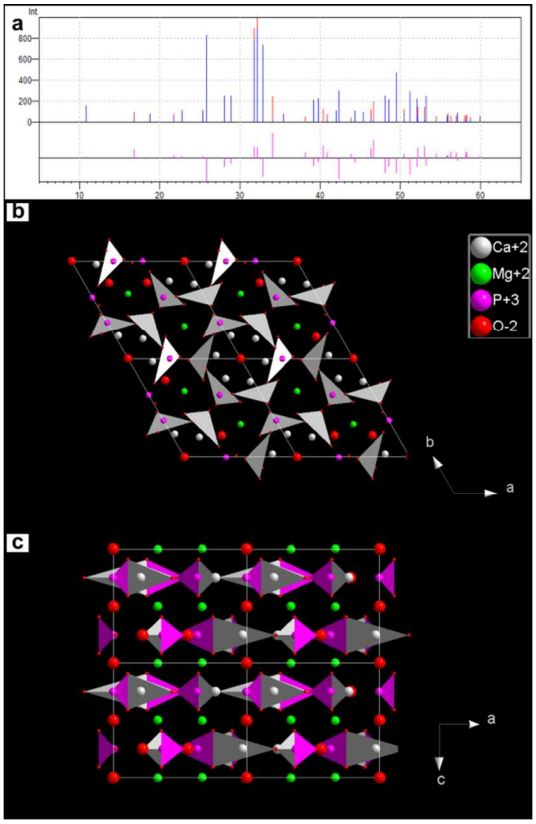

Figure 4: Molecular modeling of Mg^{2+}- substituted HA. **(a)** (Blue) theoretical XRD data, (red) experimental XRD data and (pink) correspondence of theoretical and experimental XRD data; total correlation should give a straight line. View of Mg^{2+}- HA structure along crystallographic **(b)** *c* and **(c)** *b* axis.

To achieve the favored location for Mg^{2+} occupancy on HA crystal and to predict the essential changes associated to its incorporation, crystal structure optimization [20] and Rietveld [40] refinement of pure and Mg^{2+}- substituted HA were carried out; detailed information is given in **figures S6-S9** of SI. Independently of the magnesium amount used in the synthetic route, all Mg^{2+}- HA samples better fit to the unit cell formula Ca6Mg4P6O23; theoretical representation of its crystal unit cell is shown in **figure 3b**.

Molecular modeling of HA and its Mg^{2+}- substituted counterpart structure exposes that Mg^{2+} exchange is energetically favored on the Ca(1) site, in agreement with literature information, [38] **figure 3a and 3b.** Rietveld refinement revealed fluctuations of the Mg^{2+}-HA samples unit cell in comparison with the theoretical model, **figures 4a-4c**; these differences validate the obtained altered lattice parameters, **figure 2**. Determined mean Mg-O bond distances (1.85 Å) compared with the nearest neighboring Ca-O distances (2.20 Å) decreased of about 16%. The Mg^{2+} substitution on Ca(1) site, situates the majority Mg-O bonds along the crystallographic "*a"* axis, **figure 4c**, thereby justifying the crystal cell reduction through it. There are no significant variations among crystallographic dimensions of the Mg^{2+}- HA samples related to the magnesium amount, while a significant discrepancy with the crystallographic parameters of the non-substituted HA were found. Therefore, we hypothesize that, independently of its initial starting synthesis solution concentrations, the Mg^{2+} ion was incorporated into the unit-cell of HA in a specific and limited concentration. The remainder Mg^{2+}, since no other Mg^{2+}- crystalline phases were detected, binds to the surfaces of HA crystals. Agreeing to literature evidence, the surface-bound Mg^{2+} stabilize the ACP phase and thus retard the formation and growth of HA crystals; [41] this is consistent with an increase of the amorphous phase as the amount of Mg^{2+} in the synthesis rises.

3.1.2 Morphological biomimesis: Mg^{2+}- substitution effect on nanoparticles size and shape.

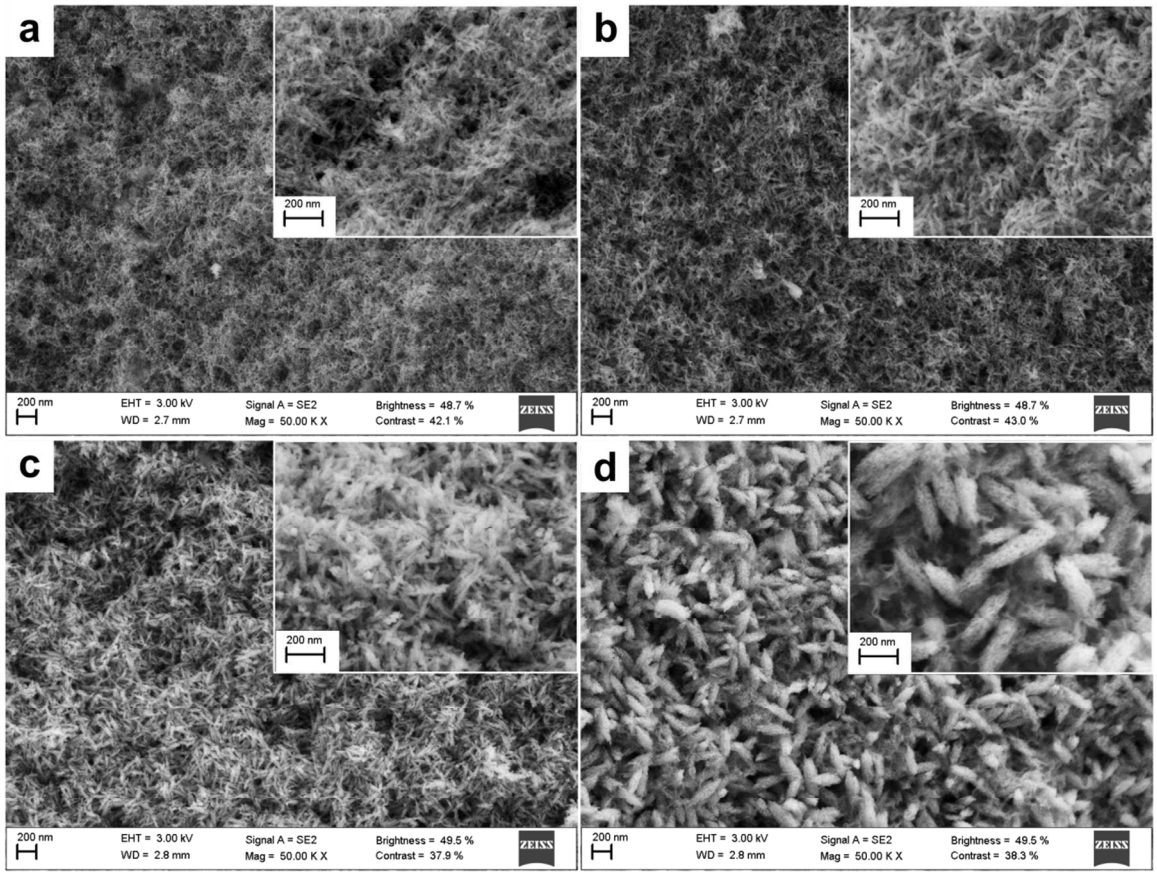

Figure 5, SEM microphotographs of different Mg^{2+}- substituted HA nano-rods. **(a)** MgI-HA (0.72 Wt% Mg); **(b)** MgII-HA (1.23 Wt% Mg); **(c)** MgIII-HA (2.46 Wt% Mg); **(d)** MgIV-HA (12.30 Wt% Mg). Scale bars: 200 nm.

All samples were obtained accordingly to a previous studied synthetic methodology[3] in which the synergistic effect of CTAB-PPG rod-like mixed micelles template combined with a hydrothermal treatment direct the assembly of HA nano-rods. To test the effect of Ca^{2+} per Mg^{2+} ions partial replacement on the morphology of the particles, the starting calcium and phosphorus sources, CTAB and PPG concentration, rate and order of reagent addition were preserved. In addition, the pH, hydrothermal aging temperature and reaction time, as well as calcination time and temperature conditions were carefully controlled and kept unaltered respect to the HA nano-rods original synthesis. [3] Microscopic inspection of

the obtained materials shows a nano-structured network created by the interconnection of rod-shape particles similarly to that formed in the non-substituted HA sample[3], **figure 5**. However, particle size distribution analysis, **figures S10-S18**, reveals an increased diameter (*d*) and length (*l*) in a directly proportional manner to the Mg^{2+} solution amount, **table 2**. In contrast to non-substituted HA, [3] TEM observations shows that Mg^{2+}- HA nanoparticles are composed by multiple small crystals embedded in an amorphous matrix. The nano-crystals organizations along different orientations as well as the grain boundaries in the amorphous phase were confirmed by H-TEM, some examples are shown in **figure 6**.

The H-TEM micrographs also demonstrate that the single crystal sizes decreased with increasing Mg^{2+} and the ACP content. In biological conditions Mg^{2+} retards the HA crystallization and increases its nucleation kinetic on collagen fibers, affecting the size and shape of mineral nuclei; [13] in terms of morphology, similar results are obtained along our investigation. In agreement with literature results, [2, 41] Mg^{2+}- substitution do not affect the nucleation frequency of HA crystals but rather only suppress the growth of precipitated crystals, resulting in the formation of numerous nano-sized HA crystals. This conclusion is consistent with the morphology of the mineral phase observed in bone tissue, [41] where without the growth restriction caused by the Mg^{2+}- substitution, the HA crystals would easily become enlarged, and the strength and flexibility characteristics of bone tissue could be lost. In addition to extended dimensions of nanoparticles, the accumulation of large amounts of Mg^{2+} provoked, as in the sample MgIV-HA, the formation of irregular pores, about 15 ± 2 nm length, organized in a bicontinuous assembly, **figure 7**.

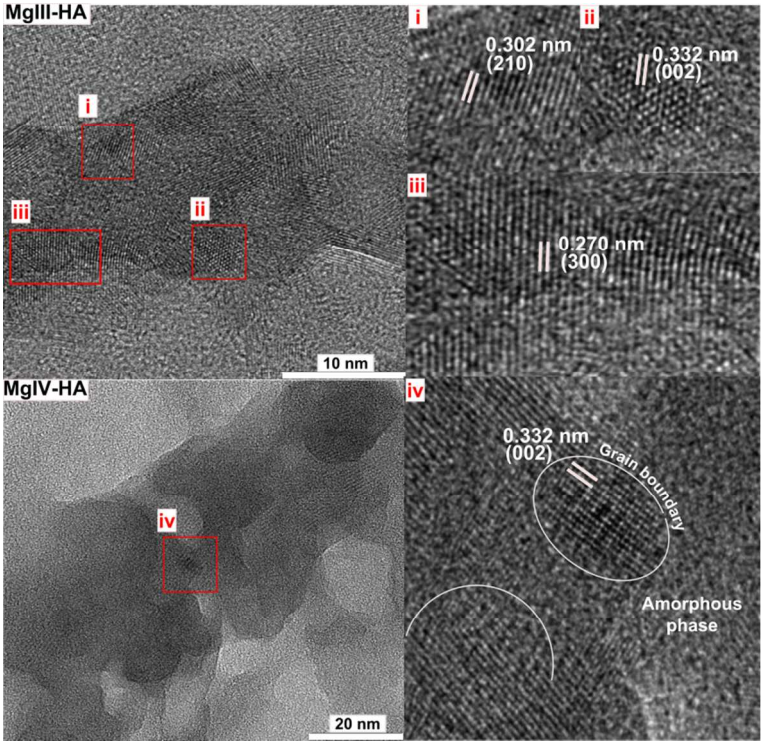

Figure 6. H-TEM microphotographs of MgIII-HA and MgIV-HA

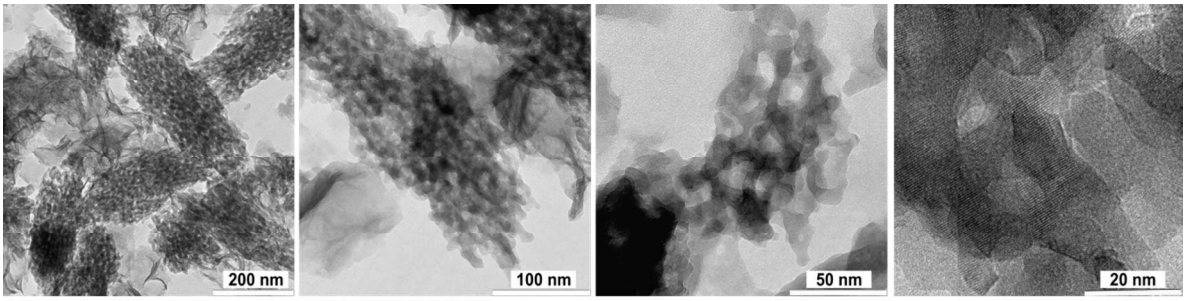

Figure 7, H-TEM microphotographs of MgIV- HA nano-rods of different magnification.

HA deposition is an intricate process that include several stages: [42] (i) formation of ACP and ionic clusters, (ii) stabilization of ACP, (iii) transformation of ACP to HA, (iv) HA crystal growth and (v) maturation. On the applied synthesis conditions, using CTAB-PPG

mixed micelles as rod-like aqueous templates through a hydrothermal treatment, PO_4^{-3} anion in the solution interact with CTA^+ cation, complementing each other in a steric and electrostatic manner, quickly replacing the Br^- ions.[3] Then, precursors react with PO_4^{-3} at the surface of CTAB-PPG mixed aggregates accordingly to the previously described five stages of HA formation, [42] leading to nano-rods structures. Our results support previous literature findings, [42] where is shown that Mg^{2+}-substitution into ACP precursor framework is limited and that it excess is adsorbed from solution onto the mineral surfaces during stage (i). As a consequence of Mg^{2+} presence, particularly the adsorbed Mg^{2+}, the life time of ACP in stage (ii) is significantly extended, the ACP to HA transformation in stage (iii) is partially inhibited and the HA crystal growth in stage (iv) is retarded [42] in a dose dependent manner. As a consequence of additional Mg^{2+} ions, the total Ca^{2+} ions in ACP is reduced and at that point fewer Ca^{2+} were release into reaction environment after the dissolution of ACP during stage (ii) causing a reduction of the supersaturating degree at the ACP/solution interface. Nucleation rate of HA during ACP to HA transformation decreased, small crystallites are produced and its subsequent aggregation lead to a large-size HA nano-rods formation. Similar results were obtained during the yttrium ion-doped hydroxyapatite tubes synthesis. [43] In addition, at maximum Mg^{2+} content, the large nano-rods exhibiting a bicontinuous porous structure can be explained by the occurrence of atomic diffusive migration at the ACP/HA interface accordingly to the Kirkerdall effect. [44] As suggested by Smigelskas and Kirkendall, [44] if there is a substantial difference between the reciprocated diffusion flux of two components in a diffusion couple, their interfacial inter-diffusion may conduce to the creation of a net directional flow of matter. As soon as the flux core to shell (J_{core}) was higher to that from shell to core (J_{shell}), the interface between core and shell progressed outward to the core, leaving vacancies behind. The accumulation of created

vacancies form a void until the reaction ended. The HA crystals nucleated and growth at the ACP/solution interface, while the preformed ACP phase provided the material flow for the conversion to HA. Geng *et al.*[45] postulated that adsorbed Mg^{2+} formed some dynamic Mg^{2+}- poor and Mg^{2+}- rich regions at the HA/ACP interface. At high Mg^{2+} concentration interfacial diffusivities are different enough to arouse the Kirkendall effect. The radial matrix flux in a process analogous to the Kirkendall phenomena has been developed for the nanoscale fabrication of a variety of hollow crystalline structures,[46] including for the phase transformation of ACP to ion-doped HA crystals.[43, 47] Some reports suggest that such mechanism may be also involved in the formation of biominerals. [47-48]

3.2 Tailored Mg^{2+}- substitution on bone repair potential

3.2.1 Surface hydration

The initial stage toward the atomistic and molecular comprehension of the devious mechanisms between biological active species and HA requires the understanding on the behavior of surface water/HA interactions. Mg^{2+}- HA powder surface hydration was analyzed by the inspection of FT-NIR spectra of adsorbed H_2O molecules, as shown in **figure 8**. All samples displays a broad band at 1928 nm that can be assigned to the combination of bending and asymmetric stretching ($\nu_2 + \nu_3$) vibrational modes of low intensity hydrogen bonded water molecules. In addition, the FT-NIR spectrum of non-substituted HA sample shows a broad adsorption band at 1420 nm that can be assigned to the combination of symmetric and asymmetric stretching ($\nu_1 + \nu_3$) vibrational modes of intermediated hydrogen-bonded water molecules, **figure 8a**. This band became narrow and of higher intensity in the spectra of the less Mg^{2+}- substituted HA samples, **figure 8b**, while practically disappeared in the high Mg^{2+}- substituted HA one, **figure 8c**.

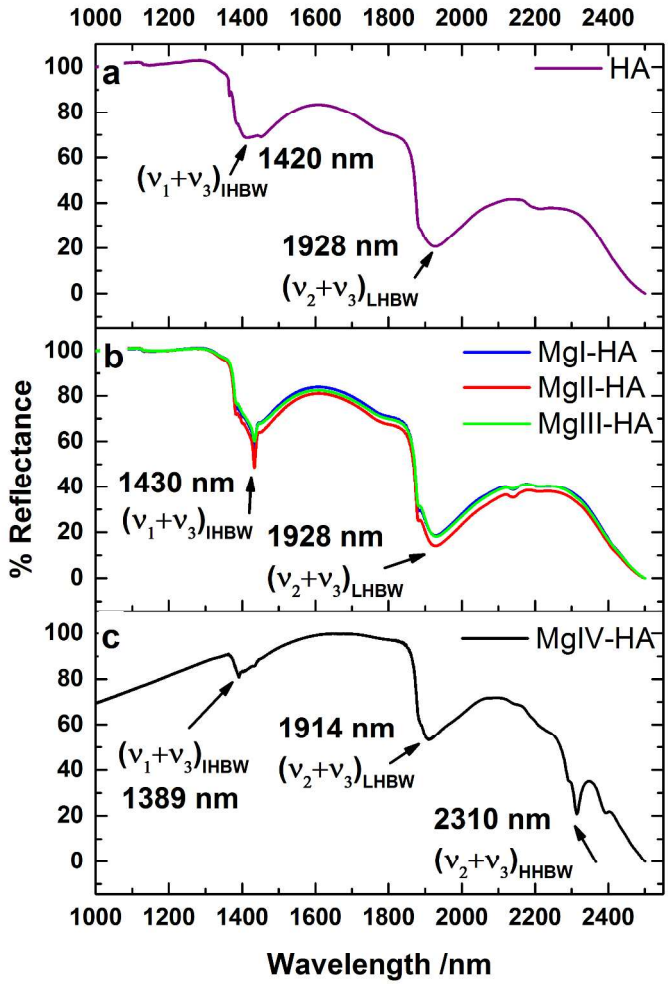

Figure 8: Near-infrared (NIR) spectra of H_2O molecules adsorbed on Mg^{2+}- HA surfaces. Symmetric stretching (ν_1); bending (ν_2); asymmetric stretching (ν_3); less hydrogen bonded water (LHBW); intermediate hydrogen bonded water (IHBW); high hydrogen bonded water (HHBW).

Finally a narrow and intense band at 2310 nm similar to that due to the (ν_2 + ν_3) vibration modes of ice was identified for MgIV-HA sample and can be associated with highly structured hydrogen bonded water molecules. Considering the overall evolution of the spectra in **figure 8**, the intensity and position variation of the broad band at 1420 nm and the presence of a narrow band at 2310 nm at the MgIV-HA spectra indicated that a multilayer of physisorbed liquid-like water was gradually restructured as a consequence of superficial Mg^{2+} presence.

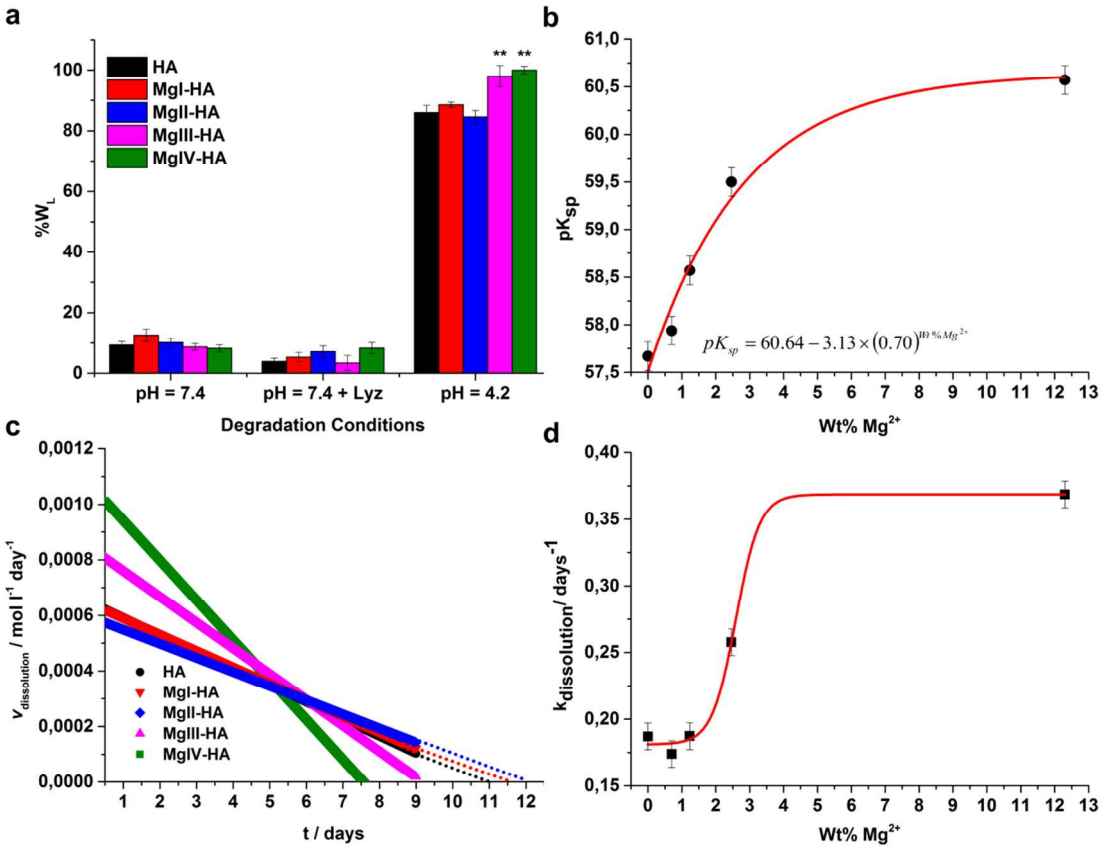

Figure 9: (a) Degradation of Mg^{2+}- HA materials under different conditions at 37°C. Results were compared with respect to HA, asterisks denote statistically significant differences (**p < 0.01). **(b)** Solubility product of different Mg^{2+}- HA materials treated under physiological conditions (pH = 7.4) at 37°C as a function of Mg^{2+} content. **(c)** Dissolution rate of different Mg^{2+}- HA materials treated under bone resorption conditions (pH = 4.2) at 37°C **(d)** Dissolution rate constant (*k*) of different Mg^{2+}- HA materials treated under bone resorption conditions (pH = 4.2) at 37°C as a function of Mg^{2+} content.

A fraction of physisorbed water, suffers a stronger interaction with the material through Mg^{2+}- bridges. Strongly held water molecules are chemisorbed on the surface acidic cationic sites of HA to form Ca^{2}+ • • • OH_2 adducts.[49-50] Since Mg^{2+} ions have a superior charge to radius ratio than Ca^{2+}, a greater water adsorption is to be expected. Consequently the formation of Mg^{2+} • • • OH_2 adducts at the crystal surface lead to appearance of new

associate bands at a less wavelength, [14] just like those observed in the case of FT-NIR spectra of the Mg^{2+}- HA samples

3.2.2 Degradation under physiological and bone resorption conditions.

In vivo, degradation of apatitic-based material occurs in two ways: (i) self-dissolution under physiological conditions and (ii) cell-mediated dissolution. The influences of Mg^{2+}-substitution on both aspects are analyzed below. The *in vitro* hydrolytic and enzymatic degradation of Mg^{2+}- HA materials, incubated at 37 °C under physiological fluid (pH = 7.4) and cell-mediated acidic conditions (pH = 4.24) were examined by the material weight loss (W_L) as a function of time during a 12 days lapse. W_L values were not statistically significant in a physiological fluid environment, neither under the effect of enzymatic degradation. Nevertheless, they degraded in a 90-100% under bone resorption conditions. The percentage of degradation depends on the amount of magnesium substitution, being higher when the latter is greater, **figure 9a**. The negligible material degradation in physiological fluids is an essential point because the biodegradation rate must be analogous to the frequency of bone tissue formation, process that take place between 8 and 16 weeks.[51] Concerning to the self-dissolution *in vivo* and *in vitro* of an apatitic implant, two main differences must be kept in mind; the dissolution process *in vivo* occurs in a thermodynamically open system whereas the *in vitro* dissolution take place in a closed system and the apatite crystal comes to equilibrium with its solubilized ions. Despite this difference, the self-dissolution rate is a function of the solubility product K_{sp}, [52] which is the equilibrium ion activity product of the materials. To further deepen into the Mg^{2+}-substitution effect on the stability of apatitic-materials in contact with physiological fluids,

their K_{sp} were analyzed. The K_{sp} is assessed for a given composition and the formula weight needs to be specified; based on our previous analysis, **table 1**, we estimate K_{sp} as following:

Non-substituted HA: $K_{sp} = [Ca^{2+}]^{9,42}\left[HPO_4{}^{-2}\right]^{0,58}\left[PO_4{}^{-3}\right]^{5,42}[OH^-]^{1,42}$

Mg^{2+}- substituted HA: $K_{sp} = [Ca^{2+}]^6[Mg^{+2}]^4\left[PO_4{}^{-3}\right]^6[OH^-]^2$

The activities of $[Ca^{2+}]$ were computed based on their measured concentrations and the Debye–Hückel limiting law,

$$-log(\gamma_i) = AZ_i^2 m^{1/2}\left(1 + Ba_i m^{1/2}\right) \quad (7)$$

where γ_i , a_i and Z_i are the activity coefficient, the effective diameter and the valence for specie i respectively; m is the total ionic strength of the solution; A = 0.51144 and B = $10^{7.515}$ are parameters for the Debye–Hückel limiting law. [52] The resultant values for all species were calculated from the chemical formulas. The relationship between the pK_{sp} and the magnesium contents in Mg^{2+}- HA samples after the immersion for 10 days at 37°C in physiological conditions fitted to an exponential curve, given by the equation: pK_{sp}= 60.64 - 3,13× (0,70) $^{Wt\%\ Mg}$, **figure 9b**, indicating that the solubility of the Mg^{2+}- HA powder as a whole decreased by increasing the magnesium content. The obtained pK_{sp} values, fluctuating from (57.67 - 60.87), are within the range of reported values in literature for enamel and HA precipitated from aqueous solutions.[53] The decrease in solubility is a result of an increased stability of Mg^{2+}- HA crystal upon magnesium incorporation.

During the processes of bone resorption and remodeling, the secretion of H^+ ions by osteoclasts offers a localized acidification to dissolve the mineral phase.[54] **Figure 9a** shows that apatitic-materials degradation under resorption conditions is highly dependent on Mg^{2+}- substitution content. Based on experimental and theoretical analysis it is postulated that dissolution of apatite in acids starts with the detachment of X^- ions as HX from the

surface.[55] Considering that a spherical bolus of material dissolves only on its surface, *S*, and that the concentration of ions in the solution is low enough that their precipitation rate on the bolus is negligible; then the rate of dissolution, $v = dS/dt$; can be written as: [56]

$$\frac{dS}{dt} = -kS \,, \tag{8}$$

where *k* is the dissolution rate.

by integration of equation (8), a relationship of surface area of the spherical bolus as a function of time can be obtained:

$$S(t) = S(0)e^{-kt} \tag{9}$$

If we consider a spherical symmetry of radius r; the surface area is $S = 4\,\pi r^2$; and the volume is $V = (4/3)\,\pi r^3$. Since the mass, *m*, of the bolus is proportional to *V*; and *S* is proportional to $V^{2/3}$; then *S* is proportional to $m^{2/3}$. Therefore, equations (8) and (9) may be rewritten as:

$$\frac{d(m)^{2/3}}{dt} = -km^{2/3} \tag{10}$$

$$m(t)^{2/3} = m(0)^{2/3}e^{-kt} \tag{11}$$

Rearranging and taking logarithms of both sides of the equality:

$$log\left(\frac{m(t)}{m(0)}\right) = -0.652kt \tag{12}$$

Hence, a plot of $log\left(\frac{m(t)}{m(0)}\right)$ *vs.* t is predicted to be a linear relationship with a negative slope of -0.652k. Confirmation of equation (12) is shown in **figure S19**.

Figures 9c and 9d show a clear increment of the dissolution rate and constant, *v* and *k,* due to Mg^{2+}- substitution. Low content of Mg^{2+}- HA powders display a similar dissolution behavior as compared to pure HA sample with a complete dissolution stipulated at 12 days of treatment. Conversely the materials with higher magnesium content, MgIII-HA and

MgIV-HA, showed a complete degradation at 9 and 7.5 days respectively. To obtain apparent solubility distributions, the dissolution rate constant (k) was plotted against Wt% Mg^{2+} and the data fitted to the sigmoidal Boltzmann equation:

$$y = A_2 + \frac{(A_1 - A_2)}{1} + exp((x - x_0)/dx), \quad (13)$$

where $y = k_{diss}$; x = Wt%Mg^{2+}; A_1 = the minimum value of y = 0,181 ± 0.009 day^{-1}; A_2 = the maximum value of y = 0.368 ± 0.010 day^{-1}; x_0 = the time point when $A_2 - A_1/2$ is reached = 2.590 ± 0.149 Wt%Mg and dx the determining width of the turnover = 0.353 ± 0.387.

As we analyzed above the dissolution kinetic of apatitic- materials in acidic media fitted to surface model dissolution in agreements with the chemical model.[55] Adsorption of protons onto calcium is impossible due to electrostatic repulsions, however, in accordance with the same model; there is an interaction between Ca^{2+} and acid anions from the solution to form calcium-acid complexes. This interaction results in the separation of some Ca^{2+} from the kink sites, after rupture of surface ≡O-Ca bonds, followed by their diffusion away from crystal phases and further into the bulk solution; the formation of a dissolution nuclei. Mg^{2+} present a higher charge to radius ratio than Ca^{2+} and consequently its presence on apatite crystal would lead to a higher electrostatic repulsion upon H^+ adsorption presence. Ionic detachment of some Mg^{2+} results in the removal of a higher local positive charge from apatite, which is instantaneously, compensated by adsorption of H^+ from the acidic solution accelerating the dissolution process. On the other hand, theoretical simulations showed that detachment of Ca^{2+} ions from Ca(1) sites of the apatite surface, those where Mg^{2+} substitution is energetically favored, should happen faster and/or more easy than that from Ca(2) sites.[57] In this way, the substitution of the Ca^{2+} ions at the Ca (1) site by Mg^{2+} drive a

faster and an energetically favored dissolution in the presence of H^+. Increasing the presence of surface Mg^{2+}, as happened for MgIII-HA and MgIV-HA materials, the number of critical nuclei is superior and crystal dissolution is accelerated.

3.2.3 Cellular - material interactions

The biocompatibility of Mg^{2+} - HA nanoparticles was tested in the presence of primary rat osteoblasts (rOBs) and endothelial cells (rECs).[58] Both types of cell are actually involved during the implant insertion and are essential to the expansion, growth, function, repair and maintenance of bone host tissue. [59-60] Osteoblasts are implicated in multifaceted interactions with a diversity of factors, mediators and cell types to form organic and non-mineralized bone matrix, [59] while endothelial cells, are directly associated to the process of vascularization through the materials.[60] Mitochondrial metabolic activity (MMA) of both cellular lines cultured during 48h in the presence of Mg^{2+}- HA powders were shown in **figures 10a** and **10b**; no statistically significant differences respects to control were observed. Although it could be appreciated a small decrease in the values observed for rOBs cultured in the presence of MgIV-HA, it was not found to be significant with respect to the other samples and for this reason was considered negligible, **figure 10a**. MMA was correlated with the cells' viability; optical microscopic observations confirm proliferation status. Cells cultured in the presence of the materials are completely adhered and no morphological statistically significant differences can be appreciated compared with control, depicting the cells were viable, **figures S20 - S22**. A deep inside to cells morphology and adhesion was performed by crystal violet staining (CVS) and immunofluorescence assays. Microscopic observations showed that rOBs exhibit a polygonal, stretched and flat shape adhered tightly to the surface, **figures 10d** and **S22**.

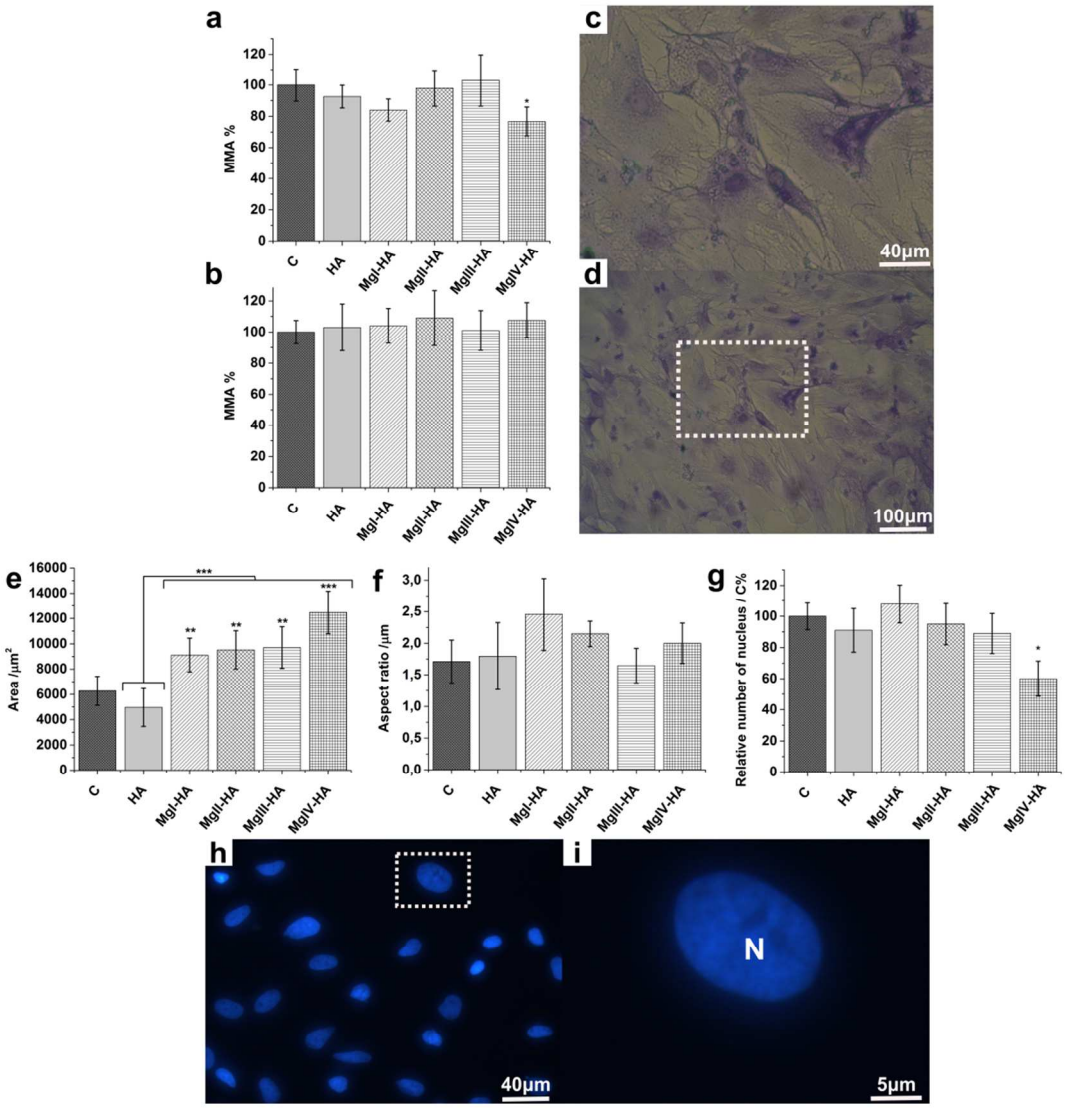

Figure 10. MMA of **(a)** rOBs and **(b)** rECs cultured in the presence of 50 µg / well Mg^{2+}-HA nanoparticles; results were expressed as percentages relative to the control (C %). **(c, d)** CVS of rOBs cultured in the presence of MI sample. **(e)** Cellular area, **(f)** major to minor axis length ratio and **(g)** amount of cellular nucleus of rOBs cultured in the presence of 50 µg / well Mg-HA nanoparticles. **(h, i)** Laser scanning confocal microphotographs showing the rOBs' nucleus morphology after culture in the presence of MgI-HA sample; **N**: nucleoli. Asterisks denote statistically significant differences (*$p < 0.05$, **$p < 0.01$; ***$p < 0.001$); differences between materials are signaled with square brackets.

High-magnification images, **figures 10c and 10i**, revealed the presence of numerous extensions, filopodia and surface anchorages, as well as a well-defined nuclear periphery. The shape, position, number of nuclei per cell, detection of micronuclei, nuclear buds and nucleoplasmic bridges where analyzed by DAPI staining as an indicator of integrity of the chromosomes, **figures 10g - 10i** and **S27**. No statistically significant differences can be observed respect to control when rOBs were cultured in the presence of Mg^{2+}- HA nanoparticles, **figures 10g.** Cytomorphometric analysis shown a homogeneous shape but a larger area of cellular extension when cells are cultured in the presence of the Mg^{2+}- HA nanoparticles compared to control and to unsubstituted HA, **figures 10e, 10f and S28**. Prior literature evidence shows that the replacement of calcium by magnesium in surface sites of the crystal exerts a synergistic effect on cell adhesion-mediating molecules [61-62] that indirectly favors the cells' anchorage and spreading, as shown in our results. A similar performance was obtained for rECs; data not shown. The obtained results confirmed a favorable cellular response, *in vitro*, in the presence of the Mg^{2+}- HA nanoparticles and therefore their biocompatibility.

Conclusion

This paper reports a systematic investigation on the regulation of the physicochemical properties of Mg^{2+}- substituted HA nanoparticles to achieve biogenic HA features with a favorable cell response *in vitro*. The concentration of Mg^{2+} used were ranged between 0.72 and 12.3 Wt % in order to mimic the physiological concentration of this ion in calcified tissues. For all samples, it was possible to obtain poor crystallized Mg^{2+}- substituted hydroxyapatite powders made up of rods-like nanoparticles with a 75 ± 5 mol% of Mg^{2+}

incorporation in the final apatite products. X-ray diffraction patterns analysis and the computed associated crystallographic parameters revealed a progressively reduction of both direct unit-cell axis and crystallinity degree as Mg^{2+}- substitution increased, reaching similar values to those present in biogenic apatite. Crystal structure optimization and Rietveld refinement indicated that all Mg^{2+}- HA samples best fixed to the Ca6Mg4P6O23 formula and that the Ca(1) site provided energetically favored positions for Mg^{2+} exchange. These facts are independently of the Mg^{2+} concentration in the material, so it is postulated that Mg^{2+} ion are incorporated to the HA unit cell in a limited and specific amount and its excess integrates the surface of the crystal. This assumption is in agreement with literature data and explains results of this study concerning to the loss of crystallinity and the associated nanoparticles morphological evolution. Increased amounts of interfacial Mg^{2+} delayed the crystallization of HA at expenses of an increased ACP phase. Hydroxyapatite crystallites became smaller, irregular, and form greater agglomerates producing nanoparticles of larger dimensions. At high concentrations of Mg^{2+} there is an interfacial ionic diffusion according to the Kirkendall's effect which causes a bicontinuous porous structure inside Mg^{2+}- HA nano-rods; a similar effect was detected during biominerals formation. Superior surface hydrations, decreased solubility in physiological media, as well as a pronounced degradation under bone resorption conditions are further associated consequences to the Mg^{2+} concentration increment in the material composition. The effects of physicochemical characteristics of the obtained nanoparticles on the cellular response were evaluated *in vitro* to test their biocompatibility. Mitochondrial metabolic activity, viability and microscopic morphological observations confirmed osteoblast and endothelial cells survival, spreading, adhesion and proliferation once they were cultured in the presence of Mg^{2+}- HA nanoparticles and no statistically significant differences respect to control

were observed. However, cytomorphometric analysis exposed a larger area of cellular extension in the presence of the Mg^{2+}- HA nanoparticles compared to control and to non-substituted HA, which was associated with the superior capacity of Mg^{2+}- substituted HA nanoparticles to favor the adsorption of cell adhesion-mediating molecules [62] from serum. The results of this work highlight the influence of Ca^{2+}- Mg^{2+} switch and validate it as a potent instrument to improve the CaPs materials performance either through modifications of its structural, morphological and chemical characteristics that can be tailored to attain biomimetic effects.

Acknowledgements: The authors acknowledge Universidad Nacional del Sur, Bahía Blanca, Argentina, (PGI 24/Q064); Concejo Nacional de Investigaciones Científicas y Técnicas (CONICET), Argentina (PIP – 11220130100100CO); Fundación Ramón Areces and Xunta de Galicia, Spain (AGRUP2015/11). NCA and NLD have postdoctoral fellowships of CONICET. AEC, VLM and PVM are researchers of CONICET.

Supporting Information (SI) available: HA and Mg-HA materials solubility in PBS, LSZ-PBS and AcOH buffer. X-ray energy dispersive (EDX) microanalysis. Rietveld refinement. Mg-HA nanoparticles size distribution histograms. Mg-HA nanoparticles degradation and cellular interactions studies: complementary information.

Table 1. Chemical information of Mg-substituted apatitic materials. (*) Computed from the amounts of Ca^{2+} and Mg^{2+} added to the initial material synthesis solutions. (§) Computed by EDX- Microanalysis results.

Sample	Wt%$^{(*)}$ Mg	Ca/Mg$^{(*)}$	Ca/Mg$^{(§)}$	Ca/P$^{(§)}$	(Ca+Mg)/P	Formula
HA (JCPDS 9-436)		---	---	1.67	1.67	$Ca_{10}(PO_4)_6OH$
Bone	0.72		35[2]	1.61[37]	1.84[37]	
Dentin	1.23		21[2]	1.61[37]	1.70[37]	
HA	---	---	---	1.53	1.53	$Ca_{9.42}(PO_4)_{5.42}(HPO_4)_{0.58}(OH)_{1.42}$
MgI-HA	0.72	39	33	1.40	1.44	$Ca_6Mg_4(PO_4)_6(OH)_2$
MgII-HA	1.23	23	18	1.40	1.47	$Ca_6Mg_4(PO_4)_6(OH)_2$
MgIII-HA	2.46	21.5	7.9	1.25	1.41	$Ca_6Mg_4(PO_4)_6(OH)_2$
MgIV-HA	12.3	2.3	1.5	1.28	1.92	$Ca_6Mg_4(PO_4)_6(OH)_2$

Table 2. Microstructural and crystallographic parameters of Mg^{2+}- substituted apatitic materials. (#) Determined from H-TEM and SEM microphotographs.

	Sample							
	HA(JCPDS 9-436)	HA	MgI-HA	MgII-HA	MgIII-HA	MgIV-HA	Bone	Dentin
X_c , eq.(2)	1	0.75 ± 0.08	0.60 ± 0.06	0.57 ± 0.06	0.49 ± 0.05	0.37 ± 0.04	0.33-0.37[37]	0.33-0.37[37]
X_c, eq. (3)	1	0.77 ± 0.08	0.65 ± 0.07	0.60 ± 0.06	0.53 ± 0.05	0.40 ± 0.04		
δ_c / nm, eq. (1)	---	40 ± 8	42 ± 8	44 ± 8	48 ± 9	51 ± 10		
δ_a / nm, eq. (1)	---	22 ± 4	20 ± 4	19 ± 4	18 ± 4	14 ± 3		
c/a	0.7306 ± 0.0073	0.7297 ± 0.0073	0.7331 ± 0.0073	0.7332 ± 0.0073	0.7310 ± 0.0073	0.7305 ± 0.0073	0.7321[37]	0.7310[37]
V / Å^3	528.6 ± 5.3	531.5 ± 5.3	526.1 ± 5.3	525.8 ± 5.3	524.1 ± 5.3	525.2 ± 5.3	528.3	529.4
$d^{(\#)}$ /nm		7.9 ± 0.7	9.9 ± 2.1	13.2 ± 2.7	27.8 ± 6.0	135.5 ± 18.3		
$l^{(\#)}$ /nm		21.6 ± 4.2	38.5 ± 10.1	68.8 ± 13.8	84.9 ± 20.5	385.2 ± 116.3		

References

(1) Lin, K.; Wu, C.; Chang, J., Advances in Synthesis of Calcium Phosphate Crystals With Controlled Size and Shape. *Acta Biomater.* **2014,** *10* (10), 4071-4102.
(2) Boanini, E.; Gazzano, M.; Bigi, A., Ionic Substitutions in Calcium Phosphates Synthesized at Low Temperature. *Acta Biomater.* **2010,** *6* (6), 1882-1894.
(3) D'Elía, N. L.; Gravina, A. N.; Ruso, J. M.; Laiuppa, J. A.; Santillán, G. E.; Messina, P. V., Manipulating the Bioactivity of Hydroxyapatite Nano-rods Structured Networks: Effects on Mineral Coating Morphology and Growth Kinetic. *Biochim. Biophys. Acta, Gen. Subj.* **2013,** *1830* (11), 5014-5026.
(4) D'Elia, N. L.; Mathieu, C.; Hoemann, C. D.; Laiuppa, J. A.; Santillan, G. E.; Messina, P. V., Bone-repair Properties of Biodegradable Hydroxyapatite Nano-rod Superstructures. *Nanoscale* **2015,** *7* (44), 18751-18762.
(5) Sartuqui, J.; D' Elía, N.; Gravina, A. N.; Messina, P. V., Analyzing the Hydrodynamic and Crowding Evolution of Aqueous Hydroxyapatite-Gelatin Networks: Digging Deeper into Bone Scaffold Design Variables. *Biopolymers* **2015,** *103* (7), 393-405.
(6) Sartuqui, J.; Gravina, A. N.; Rial, R.; Benedini, L. A.; Yahia, L. H.; Ruso, J. M.; Messina, P. V., Biomimetic Fiber Mesh Scaffolds Based on Gelatin and Hydroxyapatite Nano-rods: Designing Intrinsic Skills to Attain Bone Reparation Abilities. *Colloids Surf., B* **2016,** *145*, 382-391.
(7) Contreras-Garcia, A.; Maxime, D.; Noelia, D. e. L.; Lafantaisie-Favreau, C.-H.; Ruiz, J. C.; Rivard, G.-E.; Michel, W.; Messina, P.; Hoemann, C. D. In *Anionic Surfaces with Minimal Charge Density can Restore Burst Coagulation of Microparticle/Exosome-depleted Blood Plasma*, Frontiers in Bioengineering and Biotechnology, **2016**.
(8) Šupová, M., Substituted Hydroxyapatites for Biomedical Applications: A Review. *Ceram. Int.* **2015,** *41* (8), 9203-9231.
(9) Laurencin, D.; Almora-Barrios, N.; de Leeuw, N. H.; Gervais, C.; Bonhomme, C.; Mauri, F.; Chrzanowski, W.; Knowles, J. C.; Newport, R. J.; Wong, A., Magnesium Incorporation into Hydroxyapatite. *Biomaterials* **2011,** *32* (7), 1826-1837.
(10) Cacciotti, I.; Bianco, A.; Lombardi, M.; Montanaro, L., Mg-substituted Hydroxyapatite Nanopowders: Synthesis, Thermal Stability and Sintering Behaviour. *J. Eur. Ceram. Soc.* **2009,** *29* (14), 2969-2978.
(11) Seelig, M. S., *Magnesium Deficiency in the Pathogenesis of Disease: Early Roots of Cardiovascular, Skeletal, and Renal Abnormalities*. Springer Science & Business Media: **2012**.
(12) Rude, R. K.; Gruber, H. E., Magnesium Deficiency and Osteoporosis: Animal and Human Observations. *J. Nutr. Biochem.* **2004,** *15* (12), 710-716.
(13) Sprio, S.; Ruffini, A.; Valentini, F.; D'Alessandro, T.; Sandri, M.; Panseri, S.; Tampieri, A., Biomimesis and Biomorphic Transformations: New Concepts Applied to Bone Regeneration. *J. Biotechnol.* **2011,** *156* (4), 347-355.
(14) Bertinetti, L.; Tampieri, A.; Landi, E.; Martra, G.; Coluccia, S., Punctual Investigation of Surface Sites of HA and Magnesium-HA. *J. Eur. Ceram. Soc.* **2006,** *26* (6), 987-991.
(15) Tang, X. L.; Xiao, X. F.; Liu, R. F., Structural Characterization of Silicon-Substituted Hydroxyapatite Synthesized by a Hydrothermal Method. *Mater. Lett.* **2005,** *59* (29–30), 3841-3846.

(16) Padmanabhan, S. K.; Balakrishnan, A.; Chu, M.-C.; Lee, Y. J.; Kim, T. N.; Cho, S.-J., Sol-gel Synthesis and Characterization of Hydroxyapatite Nanorods. *Particulology* **2009,** *7*, 466-470.

(17) Bouyer, E.; Gitzhofer, F.; Boulos, M., Morphological Study of Hydroxyapatite Nanocrystal Suspension. *J. Mater. Sci.: Mater. Med.* **2000,** *11* (8), 523-531.

(18) Tilley, R. J., *Crystals and crystal structures*. John Wiley & Sons: **2006**.

(19) Hunter, B. A. In *Rietica - a visual Rietveld program*, 2nd AINSE Symposium on Neutron Scattering Powder Diffraction and Australian Neutron Beam users group meeting Symposium handbook, Australia, Australia, **2000**; p 24.

(20) Putz, H.; Schön, J.; Jansen, M., Combined Method for Ab Initio Structure Solution from Powder Diffraction Data. *J. Appl. Crystallogr.* **1999,** *32* (5), 864-870.

(21) Baron, R.; Neff, L.; Louvard, D.; Courtoy, P. J., Cell-mediated Extracellular Acidification and Bone Resorption: Evidence for a Low pH in Resorbing Lacunae and Localization of a 100-kD Lysosomal Membrane Protein at the Osteoclast Ruffled Border. *J. Cell Biol.* **1985,** *101* (6), 2210-2222.

(22) Matsumoto, T.; Okazaki, M.; Inoue, M.; Yamaguchi, S.; Kusunose, T.; Toyonaga, T.; Hamada, Y.; Takahashi, J., Hydroxyapatite Particles as a Controlled Release Carrier of Protein. *Biomaterials* **2004,** *25* (17), 3807-3812.

(23) Costa-Pinto, A. R.; Martins, A. M.; Castelhano-Carlos, M. J.; Correlo, V. M.; Sol, P. C.; Longatto-Filho, A.; Battacharya, M.; Reis, R. L.; Neves, N. M., In Vitro Degradation and in Vivo Biocompatibility of Chitosan–poly (butylene succinate) Fiber Mesh Scaffolds. *J. Bioact. Compat. Polym.* **2014,** *29* (2), 137-151.

(24) Tampieri, A.; Iafisco, M.; Sandri, M.; Panseri, S.; Cunha, C.; Sprio, S.; Savini, E.; Uhlarz, M.; Herrmannsdörfer, T., Magnetic Bioinspired Hybrid Nanostructured Collagen–Hydroxyapatite Scaffolds Supporting Cell Proliferation and Tuning Regenerative Process. *ACS Appl. Mater. Interfaces* **2014,** *6* (18), 15697-15707.

(25) Fulmer, M. T.; Ison, I. C.; Hankermayer, C. R.; Constantz, B. R.; Ross, J., Measurements of the Solubilities and Sissolution Rates of Several Hydroxyapatites. *Biomaterials* **2002,** *23* (3), 751-755.

(26) Yeh, Y. C.; Hwang, G. Y.; Liu, I. P.; Yang, V. C., Identification and Expression of Scavenger Receptor SR-BI in Endothelial Cells and Smooth Muscle Cells of Rat Aorta in Vitro and in Vivo. *Atherosclerosis 161* (1), 95-103.

(27) Campelo, A. E.; Cutini, P. H.; Massheimer, V. L., Cellular Actions of Testosterone in Vascular Cells: Mechanism Independent of Aromatization to Estradiol. *Steroids* **2012,** *77* (11), 1033-1040

(28) National Research Council, *Guide for the Care and Use of Laboratory Animals*. National Academies Press: **2010**.

(29) Marshall, N. J.; Goodwin, C. J.; Holt, S. J., A Critical Assessment of the use of Microculture Tetrazolium Assays to Measure Cell Growth and Function. *Growth Regul.* **1995,** *5* (2), 69-84.

(30) Riss TL; Moravec RA; Niles AL; Benink HA; Worzella TJ; L, M., Cell Viability Assays. Assay Guidance Manual [Internet]. Sittampalam GS, C. N., Nelson H, Ed. Eli Lilly & Company and the National Center for Advancing Translational Sciences; 2004-. Available from: http://www.ncbi.nlm.nih.gov/books/NBK144065/: **2013**. http://www.ncbi.nlm.nih.gov/books/NBK144065.

(31) Denizot, F.; Lang, R., Rapid Colorimetric Assay for Cell Growth and Survival: Modifications to the Tetrazolium Dye Procedure Giving Improved Sensitivity and Reliability. *J. Immunol. Methods* **1986,** *89* (2), 271-277.

(32) Feoktistova, M.; Geserick, P.; Leverkus, M., Crystal Violet Assay for Determining Viability of Cultured Cells. *Cold Spring Harbor Protocols* **2016,** *2016* (4), pdb. prot087379.

(33) Foldberg, S.; Petersen, M.; Fojan, P.; Gurevich, L.; Fink, T.; Pennisi, C. P.; Zachar, V., Patterned Poly(lactic acid) Films Support Growth and Spontaneous Multilineage Gene Expression of Adipose-derived Stem Cells. *Colloids Surf., B* **2012,** *93*, 92-99.

(34) Cutini, P. H.; Campelo, A. E.; Massheimer, V. L., Differential Regulation of Endothelium Behavior by Progesterone and Medroxyprogesterone Acetate. *J. Endocrinol.* **2014,** *220* (3), 179-193.

(35) Meneghini, C.; Dalconi, M. C.; Nuzzo, S.; Mobilio, S.; Wenk, R. H., Rietveld Refinement on X-ray Diffraction Patterns of Bioapatite in Human Fetal Bones. *Biophys. J.* **2003,** *84* (3), 2021-2029.

(36) Dorozhkin, S. V., Nanodimensional and Nanocrystalline Apatites and Other Calcium Orthophosphates in Biomedical Engineering, Biology and Medicine. *Materials* **2009,** *2* (4), 1975-2045.

(37) Dorozhkin, S. V., Calcium Orthophosphates: Occurrence, Properties, Biomineralization, Pathological Calcification and Biomimetic Applications. *Biomatter.* **2011,** *1* (2), 121-164.

(38) Ren, F.; Leng, Y.; Xin, R.; Ge, X., Synthesis, Characterization and Ab Initio Simulation of Magnesium-Substituted Hydroxyapatite. *Acta Biomater.* **2010,** *6* (7), 2787-2796.

(39) Farzadi, A.; Bakhshi, F.; Solati-Hashjin, M.; Asadi-Eydivand, M.; abu Osman, N. A., Magnesium Incorporated Hydroxyapatite: Synthesis and Structural Properties Characterization. *Ceram. Int.* **2014,** *40* (4), 6021-6029.

(40) Rietveld, H., A Profile Refinement Method for Nuclear and Magnetic Structures. *J. Appl. Crystallogr.* **1969,** *2* (2), 65-71.

(41) Lakhkar, N. J.; Lee, I.-H.; Kim, H.-W.; Salih, V.; Wall, I. B.; Knowles, J. C., Bone Formation Controlled by Biologically Relevant Inorganic Ions: Role and Controlled Delivery from Phosphate-Based Glasses. *Adv. Drug Delivery Rev.* **2013,** *65* (4), 405-420.

(42) Ding, H.; Pan, H.; Xu, X.; Tang, R., Toward a Detailed Understanding of Magnesium ions on Hydroxyapatite Crystallization Inhibition. *Cryst. Growth Des.* **2014,** *14* (2), 763-769.

(43) Li, C.; Ge, X.; Li, G.; Lu, H.; Ding, R., In Situ Hydrothermal Crystallization of Hexagonal Hydroxyapatite Tubes from Yttrium Ion-doped Hydroxyapatite by the Kirkendall Effect. *Mater. Sci. Eng.,C* **2014,** *45*, 191-195.

(44) Kirkendall, E., Diffusion of Zinc in Alpha Brass. *Aime. Trans.* **1942,** *147*, 104-109.

(45) Geng, Z.; Cui, Z.; Li, Z.; Zhu, S.; Liang, Y.; Lu, W. W.; Yang, X., Synthesis, Characterization and the Formation Mechanism of Magnesium- and Strontium-substituted Hydroxyapatite. *J. Mater. Chem. B* **2015,** *3* (18), 3738-3746.

(46) Liu, B.; Zeng, H. C., Fabrication of ZnO "Dandelions" via a Modified Kirkendall Process. *J. Am. Chem. Soc.* **2004,** *126* (51), 16744-16746.

(47) Tao, J.; Pan, H.; Wang, J.; Wu, J.; Wang, B.; Xu, X.; Tang, R., Evolution of Amorphous Calcium Phosphate to Hydroxyapatite Probed by Gold Nanoparticles. *J. Phys. Chem. C* **2008,** *112* (38), 14929-14933.

(48) Li, G.; Huang, H.; Yu, B.; Wang, Y.; Tao, J.; Wei, Y.; Li, S.; Liu, Z.; Xu, Y.; Xu, R., A Bioscaffolding Strategy for Hierarchical Zeolites with a Nanotube-trimodal Network. *Chem. Sci.* **2016,** *7* (2), 1582-1587.

(49) Chiatti, F.; Delle Piane, M.; Ugliengo, P.; Corno, M., Water at Hydroxyapatite Surfaces: the Effect of Coverage and Surface Termination as Investigated by All-electron B3LYP-D* Simulations. *Theor. Chem. Acc.* **2016,** *135* (3), 1-15.

(50) Corno, M.; Busco, C.; Bolis, V.; Tosoni, S.; Ugliengo, P., Water Adsorption on the Stoichiometric (001) and (010) Surfaces of Hydroxyapatite: A Periodic B3LYP Study. *Langmuir* **2009,** *25* (4), 2188-2198.

(51) Urist, M. R., Bone: Formation by Autoinduction. *Science* **1965,** *150* (3698), 893-899.

(52) Li, X.; Ito, A.; Sogo, Y.; Wang, X.; LeGeros, R., Solubility of Mg-containing β-tricalcium Phosphate at 25 C. *Acta Biomater.* **2009,** *5* (1), 508-517.

(53) Shellis, R. P.; Wilson, R. M., Apparent Solubility Distributions of Hydroxyapatite and Enamel Apatite. *J. Colloid Interface Sci.* **2004,** *278* (2), 325-332.

(54) Vaes, G., Cellular Biology and Biochemical Mechanism of Bone Resorption: A Review of Recent Developments on the Formation, Activation, and Mode of Action of Osteoclasts. *Clin. Orthop. Relat. Res.* **1988,** *231*, 239-271.

(55) Dorozhkin, S. V., Dissolution Mechanism of Calcium Apatites in Acids: A Review of Literature. *World J Methodol.* **2012,** *2* (1), 1-17.

(56) Hankermeyer, C. R.; Ohashi, K. L.; Delaney, D. C.; Ross, J.; Constantz, B. R., Dissolution Rates of Carbonated Hydroxyapatite in Hydrochloric Acid. *Biomaterials* **2002,** *23* (3), 743-750.

(57) Hochrein, O.; Zahn, D., On the Molecular Mechanisms of the Acid-induced Dissociation of Hydroxyapatite in Water. *J. Mol. Model.* **2011,** *17* (6), 1525-1528.

(58) Hamilton, D. W.; Chehroudi, B.; Brunette, D. M., Comparative Response of Epithelial Cells and Osteoblasts to Microfabricated Tapered Pit Topographies in Vitro and in Vivo. *Biomaterials* **2007,** *28* (14), 2281-2293.

(59) Jayakumar, P.; Di Silvio, L.; Tanner, K. E.; Dalby, M. J., Osteoblasts in Bone Tissue Engineering. *Proc. Inst. Mech. Eng., Part H* **2010,** *224* (12), 1415-1440.

(60) Santos, M. I.; Tuzlakoglu, K.; Fuchs, S.; Gomes, M. E.; Peters, K.; Unger, R. E.; Piskin, E.; Reis, R. L.; Kirkpatrick, C. J., Endothelial Cell Colonization and Angiogenic Potential of Combined Nano- and Micro-fibrous Scaffolds for Bone Tissue Engineering. *Biomaterials* **2008,** *29* (32), 4306-4313.

(61) Zreiqat, H.; Howlett, C.; Zannettino, A.; Evans, P.; Schulze□Tanzil, G.; Knabe, C.; Shakibaei, M., Mechanisms of Magnesium□stimulated Adhesion of Osteoblastic Cells to Commonly Used Orthopaedic Implants. *J. Biomed. Mater. Res.* **2002,** *62* (2), 175-184.

(62) Huang, B.; Yuan, Y.; Li, T.; Ding, S.; Zhang, W.; Gu, Y.; Liu, C., Facilitated Receptor-recognition and Enhanced Bioactivity of Bone Morphogenetic Protein-2 on Magnesium-substituted Hydroxyapatite Surface. *Sci. Rep.* **2016,** *6*, 24323.

Table of Contents Graphic (TOC)